AIP | Physics of Plasmas
#1 JOURNAL IN 2014 GOOGLE SCHOLAR METRICS FOR THE PLASMA & FUSION CATEGORY

Influence of centrifugal effects on particle and momentum transport in National Spherical Torus Experiment

R. Buchholz, S. Grosshauser, W. Guttenfelder, W. A. Hornsby, P. Migliano, A. G. Peeters, and D. Strintzi

Citation: Physics of Plasmas **22**, 082307 (2015); doi: 10.1063/1.4928427
View online: http://dx.doi.org/10.1063/1.4928427
View Table of Contents: http://scitation.aip.org/content/aip/journal/pop/22/8?ver=pdfcov
Published by the AIP Publishing

Articles you may be interested in

The effects of dilution on turbulence and transport in C-Mod ohmic plasmas and comparisons with gyrokinetic simulations
Phys. Plasmas **22**, 072507 (2015); 10.1063/1.4926518

Characterization and parametric dependencies of low wavenumber pedestal turbulence in the National Spherical Torus Experimenta)
Phys. Plasmas **20**, 055903 (2013); 10.1063/1.4803913

Suppressing electron turbulence and triggering internal transport barriers with reversed magnetic shear in the National Spherical Torus Experimenta)
Phys. Plasmas **19**, 056120 (2012); 10.1063/1.4718456

Scaling of linear microtearing stability for a high collisionality National Spherical Torus Experiment discharge
Phys. Plasmas **19**, 022506 (2012); 10.1063/1.3685698

Carbon ion plume emission produced by charge exchange with neutral beams on National Spherical Torus Experiment
Rev. Sci. Instrum. **77**, 10E902 (2006); 10.1063/1.2217012

TREK
www.trekinc.com

HIGH-VOLTAGE AMPLIFIERS AND ELECTROSTATIC VOLTMETERS
ENABLING RESEARCH AND INNOVATION IN DIELECTRICS, MICROFLUIDICS, MATERIALS, PLASMAS AND PIEZOS

This article is copyrighted as indicated in the article. Reuse of AIP content is subject to the terms at: http://scitation.aip.org/termsconditions. Downloaded to IP: 198.125.231.54 On: Wed, 30 Sep 2015 20:20:01

Influence of centrifugal effects on particle and momentum transport in National Spherical Torus Experiment

R. Buchholz,[1] S. Grosshauser,[1] W. Guttenfelder,[2] W. A. Hornsby,[1] P. Migliano,[1] A. G. Peeters,[1] and D. Strintzi[1]
[1]Physics Department, University of Bayreuth, Universitätsstrasse 30 Bayreuth, Germany
[2]Princeton Plasma Physics Laboratory, Princeton, New Jersey 08543, USA

(Received 22 June 2015; accepted 23 July 2015; published online 14 August 2015)

This paper studies the effect of rotation on microinstabilities under experimentally relevant conditions in the spherical tokamak National Spherical Torus Experiment (NSTX). The focus is specifically on the centrifugal force effects on the impurity and momentum transport in the core ($r/a = 0.7$) of an H-mode plasma. Due to relatively high beta, the linear simulations predict the presence of both microtearing mode (MTM) and hybrid ion temperature gradient-kinetic ballooning mode (ITG-KBM) electromagnetic instabilities. Rotation effects on both MTM and ITG-KBM growth rates and mode frequencies are found to be small for the experimental values. However, they do influence the quasi-linear particle and momentum fluxes predicted by ITG-KBM (MTM contributes only to electron heat flux). The gradient of the intrinsic carbon impurity in the source-free core region is predicted to be locally hollow, strengthened by centrifugal effects. This result is consistent with experimental measurements and contradicts neoclassical theory that typically provides a reasonable explanation of the impurity profiles in NSTX. The diffusive and Coriolis pinch contributions to momentum transport are found to be relatively weak. Surprisingly, the strongest contribution derives from a centrifugal effect proportional to the product of rotation and rotation shear, which predicts an inward momentum flux roughly three times bigger than the Coriolis pinch, suggesting it should be considered when interpreting previous experimental pinch measurements.
© 2015 AIP Publishing LLC. [http://dx.doi.org/10.1063/1.4928427]

I. INTRODUCTION

Flow shear in tokamaks has been predicted to contribute to a number of effects in turbulent transport. For example, sheared perpendicular $E \times B$ flows can suppress turbulence,[1] while sheared parallel flow can drive diffusive momentum transport[2] and destabilize Kelvin-Helmholtz instabilities.[3] Work in recent years has demonstrated that toroidal rotation (in the absence of shear) can also have significant influence on particle, heat, and momentum transport from microturbulence due to many physical mechanisms. For example, finite toroidal flow allows for a momentum pinch through the Coriolis effect,[4] which can also influence particle and impurity transport through roto-diffusion (a flux proportional to the gradient of the rotation velocity).[5,6] For increasingly large Mach numbers, centrifugal effects influence momentum and impurity transport and growth rates of the underlying instabilities. This occurs due to changes in both perpendicular particle drifts and particle trapping through the variation of the equilibrium potential around a flux surface.[5,7] Heavier impurities are expected to be more influenced due to their higher mass, smaller thermal velocities, and correspondingly higher Mach number. Furthermore, it was found that effects due to rotation can depend not just on toroidal flow but also on the product of toroidal flow and flow shear.[5]

In this paper, we investigate the influence of centrifugal effects on particle and momentum transport in National Spherical Torus Experiment (NSTX)[8] H-mode plasmas. As a spherical tokamak (ST),[9,10] NSTX provides a unique test of microstability theory as it operates at lower aspect ratio ($R/a \sim 1.5$) and relatively large beta

$$\beta_{ref} = \frac{2\mu_0 n_{ref} T_{ref}}{B_{ref}^2}, \tag{1}$$

compared to conventional aspect ratio tokamaks. Because of the reduced aspect ratio and corresponding lower moment of inertia, STs can rotate rapidly due to the momentum injected via neutral beam heating. Furthermore, due to the high beta, strong surface shaping, and large perpendicular $E \times B$ flow shear, electrostatic microinstabilities, such as ion temperature gradient (ITG) and the trapped electron mode (TEM), are often predicted to be suppressed[11] or stable entirely (in the absence of $E \times B$ shear) so that other instabilities must be considered.[12] The fact that ion thermal transport in H-modes is typically found to be close to neoclassical predictions is consistent with this interpretation.

Fig. 1 shows the normalized toroidal rotation ($Mach = u = R\Omega/c_s$, here $c_s = \sqrt{T_{ref}/m_{ref}}$) and toroidal rotation shear ($u' = -R^2\nabla\Omega/c_s$) for various NSTX H-modes at three radii (r/a = 0.6, 0.7, and 0.8).

As expected, towards the core, the rotation velocities are usually higher, and there is a significant variation in the rotation velocity at $r/a = 0.7$ depending on the plasma parameters. In the region of interest ($r/a = 0.6 - 0.8$), the Mach number of deuterium is significantly below one but, of course, the Mach number of the impurity species is larger compared to that of deuterium ($M_Z = M_D\sqrt{m_Z/m_D}$). For

 © 2015 AIP Publishing LLC

This article is copyrighted as indicated in the article. Reuse of AIP content is subject to the terms at: http://scitation.aip.org/termsconditions. Downloaded to IP: 198.125.231.54 On: Wed, 30 Sep 2015 20:20:01

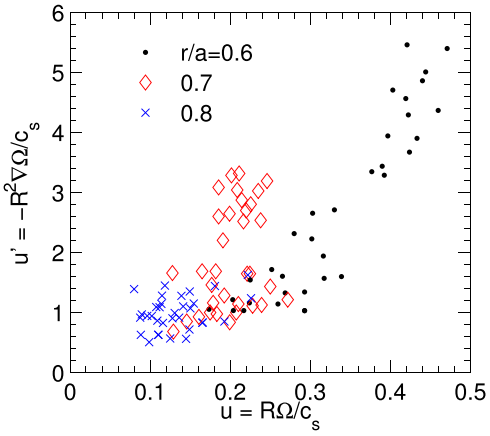

FIG. 1. Plot of rotational gradient vs. rotation velocity of different shots of NSTX, at three different radial positions (GYRO units). A trend to higher rotation velocities closer to the axis is also observable.

comparison, results for the rotation velocity and gradients of AUG H-modes have been presented in Ref. 13. They found values of u_B up to 0.5 and u'_B up to 1.9 for boron (values are scaled to the units used in Fig. 1 and to deuterium) at $r/a = 0.5$.

The present study is motivated by recent observations of impurity transport in NSTX H-modes.[18] In earlier experiments, impurity transport in NSTX was found to be described by neoclassical theory, especially for perturbative measurements using injected trace impurities such as neon.[14–16] This was also found to be the case for the intrinsic carbon impurity (NSTX walls were covered with graphite tiles) in ELMy H-modes. The fact that impurity transport seems to be governed by neoclassical theory suggests turbulence is too weak to contribute, which is consistent with the ion thermal transport also being close to neoclassical predictions.

However, in discharges where lithium has been applied to the divertor region, confinement improves with an increase in temperature, and the structure of the H-mode pedestal changes in a way that the discharges become edge localized mode (ELM)-free.[17] As a result, carbon begins to accumulate, leading to plasmas with $Z_{eff} = 2 - 4$. However, detailed analysis shows that the carbon profiles in these ELM-free discharges are inconsistent with neoclassical theory outside the mid-radius ($r/a > 0.6$).[18] In particular, neoclassical theory predicts there should be a strong pinch (and therefore peaked carbon profile, or $R/L_{n,c} > 0$ where $R/L_n = -R/n\nabla n$) at $r/a = 0.7$ while experimentally a hollow profile is measured ($R/L_{n,c} < 0$). In addition, the ion thermal transport in these lithiated, high temperature (lower collisionality) plasmas appears to begin departing from neoclassical predictions.[19] It is therefore of interest to investigate the microstability properties of these plasmas and the corresponding predicted impurity transport.

Linear gyrokinetic analysis for similar lithiated discharges at low collisionality find that in this radial region the microtearing mode (MTM) and kinetic ballooning mode (KBM) are the only unstable instabilities.[12,19] It is important to note that these instabilities are fundamentally electromagnetic in nature, both depending on shear magnetic perturbations, while the KBM for these high beta conditions also depends on compressional magnetic perturbations. Linear and nonlinear simulations of the MTM predict that it only transports electron heat flux and its contributions to particle and momentum fluxes are negligible.[21–24] Therefore, we focus on linear analysis of the KBM and corresponding quasilinear predictions of the particle transport, assuming it influences transport even in the presence of a stronger microtearing instability. Nonlinear simulations have been left for future investigations.

The structure of this paper is as follows. In Sec. II, the parameters for the simulations are given, as well as the results of a benchmark between GKW and GYRO. The nature of the unstable modes present in the simulations is discussed in Sec. III, followed by the results for the particle and momentum transport in Secs. IV and V, respectively. The conclusions are then drawn in Sec. VI

II. NUMERICAL SETUP AND BENCHMARK

A short overview of the simulation setup (parameters and grid size) is given below. Two different NSTX shots have been considered, shot numbers 129064 and 129061. The shots are lithium-conditioned, ELM-free, H-mode discharges with NBI (neutral beam injection)-heating. The former has been used for a benchmark between the two gyrokinetic codes GYRO[25] and GKW,[26] while the second has been used in the investigation of the effects of plasma rotation. Table I lists the base simulation parameters for the two cases, and Tables II and III the species parameters. Two different cases have been used for the benchmark. The first considers only electrostatic effects and no collisions, while the

TABLE I. Base parameters for the simulations.

Property	#129064	#129061
$t_{\text{shot}}(s)$		0.45
ϵ	0.436	0.434
r/a	0.7	0.7
q	3.50	3.49
$\hat{s}$	1.45	1.47
κ	2.26	2.27
δ	0.249	0.250
ζ	−0.0170	−0.0160
R_{mil}	1.0	1.0
Z_{mil}	−0.0175	−0.0178
$d\kappa/d\psi$	0.0122	0.0152
$d\delta/d\psi$	0.330	0.323
$d\zeta/d\psi$	0.128	0.107
$dR_{\text{mil}}/d\psi$	−0.358	−0.360
$dZ_{\text{mil}}/d\psi$	−0.0286	−0.0408
$B_{ref}(T)$	1.150	1.150
β_{ref}	7.13×10^{-2}	7.39×10^{-2}
β'_{ref}	-9.95×10^{-1}	-6.22×10^{-1}
$R_{\text{ref}}(m)$	0.950	0.948
$T_{\text{ref}} = T_e(keV)$	0.704	0.634
$n_{\text{ref}} = n_e(10^{19}m^{-3})$	3.87	4.52
$Z_{\text{eff}}(1)$	1.0	1.0
u	0.0	0.136
u′	0.0	0.910

This article is copyrighted as indicated in the article. Reuse of AIP content is subject to the terms at: http://scitation.aip.org/termsconditions. Downloaded to IP: 198.125.231.54 On: Wed, 30 Sep 2015 20:20:01

TABLE II. Species parameters of shot 129 064. Note that these are rounded values and small adjustments for density and density gradient length might be necessary for quasi-neutrality.

Property	Deuterium	Carbon	Electrons
m_i/m_{ref}	1.0	5.97	2.72×10^{-4}
Z_i	1	6	−1
T_i/T_{ref}	0.985	0.985	1.0
n_i/n_{ref}	0.494	0.0843	1.0
R/L_T	3.47	3.47	5.78
R/L_n	7.52	−2.00	2.70

TABLE III. Species parameters of shot 129 061. Note that these are rounded values and small adjustments for density and density gradient length might be necessary for quasi-neutrality.

Property	Deuterium	Carbon	Electrons	Tungsten
m_i/m_{ref}	1.0	5.97	2.72×10^{-4}	91.3
Z_i	1	6	−1	39
T_i/T_{ref}	0.859	0.859	1.0	0.859
n_i/n_{ref}	0.511	0.0814	1.0	0.0
R/L_T	4.04	4.04	4.33	4.04
R/L_n	4.22	−3.54	0.426	0.0

second includes collisions and electromagnetic effects. Due to the different definitions of the wave vector $k_\theta\rho$ in GKW

$$(k_\theta\rho_{ref})^2 = g^{\zeta\zeta}k_\zeta^2, \tag{2}$$

$$g^{\zeta\zeta} = \left(\frac{\partial\zeta}{\partial r}\right)^2 g^{rr} + \left(\frac{\partial\zeta}{\partial\theta}\right)^2 g^{\theta\theta} + 2\frac{\partial\zeta}{\partial r}\frac{\partial\zeta}{\partial\theta}g^{r\theta} + \frac{1}{4\pi^2}g^{\phi\phi} \tag{3}$$

($\rho_{ref} = m_{ref}v_{thref}/eB_{ref}$ and g is the metric tensor) and GYRO, a conversion is necessary. The conversion factor is

$$\frac{(k_\theta\rho_{s,unit})_{gyro}}{(k_\theta\rho_{ref})_{gkw}} = \frac{\sqrt{2}\mathcal{E}^{\psi\zeta}}{s_j\sqrt{g^{\zeta\zeta}}}, \tag{4}$$

with $s_j = \mathrm{sign}(j\cdot\nabla\phi)$ and with the tensor element $\mathcal{E}^{\psi\zeta} = \frac{s_j}{4\pi}\frac{\partial\psi}{\partial\Psi}$ (Ψ is the normalized poloidal flux).

The results of the comparison can be seen in Fig. 2 (this and the following figures use values normalized as in GKW). The agreement between the two codes is good, in the simplified and in the elaborate case. In the simplified version, an ITG mode is found. The second benchmark has a MTM at small $k_\theta\rho$, while at higher wave numbers, there is a KBM. For the KBM, there are some small differences in growth rate. However, for the critical wave-number $k_\theta\rho$, where the transition between dominant mode occurs, agreement between the two codes is achieved.

The various geometry parameters in Table I refer to the Miller geometry,[27] which has been chosen as a trade-off between effort and accuracy. In Miller geometry, the cross section is described by

$$R = R_{mil} + \psi\cos(\theta + \arcsin\delta\sin\theta), \tag{5}$$

$$Z = Z_{mil} + \psi\kappa\sin(\theta + \zeta\sin 2\theta), \tag{6}$$

Z_{mil} and R_{mil} are offsets of the center of the surface, with respect to the magnetic axis and normalized to R_{ref}. The parameters κ, *delta*, and ζ describe the elongation, triangularity, and squareness of the surface, respectively. Note that the radial coordinate, ψ, in GKW is scaled with the reference radius

$$\psi = \frac{r}{R_{ref}}. \tag{7}$$

Electro-magnetic effects, including the effect of compressibility, and collisions (pitch angle scattering only) have been taken into account. The β value has already been defined in Eq. (1). Its derivative is defined as

$$\beta'_{ref} = -\beta_{ref}\sum_s n_{N,s}T_{N,s}\left(\frac{R}{L_{n_s}} + \frac{R}{L_{T_s}}\right) \tag{8}$$

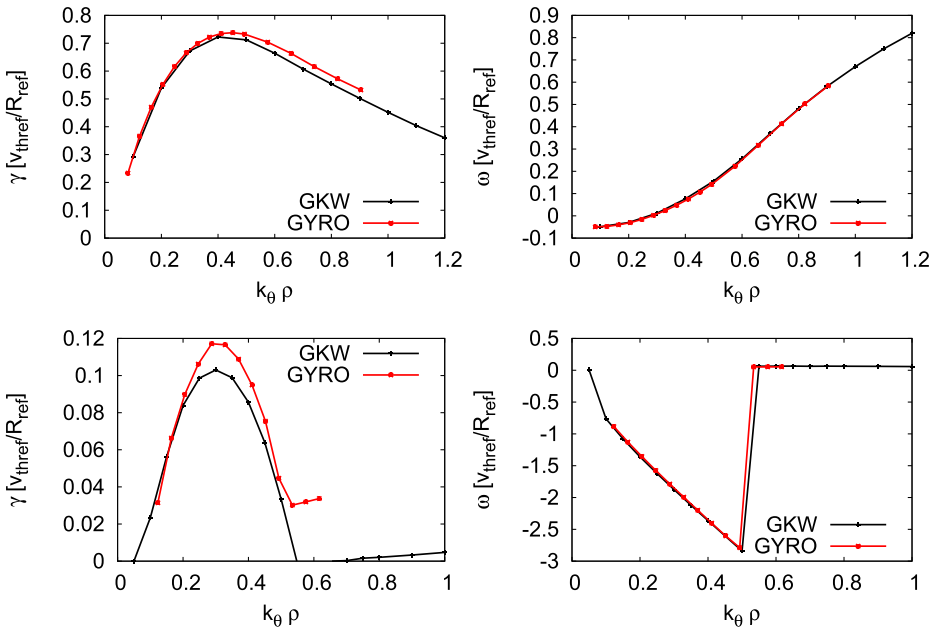

FIG. 2. Comparison of the results from GYRO and GKW. Upper row is for a simplified case without electromagnetic effects, collisions, or compressional effects, while the lower includes these effects. As can bee seen, the agreement of the codes is good.

This article is copyrighted as indicated in the article. Reuse of AIP content is subject to the terms at: http://scitation.aip.org/termsconditions. Downloaded to IP: 198.125.231.54 On: Wed, 30 Sep 2015 20:20:01

(sum over species, n_N/T_N is normalized to reference density/temperature) and the reference collision frequency is

$$\nu_{ref} = 6.5141 \cdot 10^{-5} R_{ref} n_{ref}^{19} \frac{\ln \Lambda^{i/i}}{T_{ref}^2}. \tag{9}$$

The gyrokinetic equations, formulated in a rotating frame, used by GKW can be found in Refs. 4 and 26, and the changes to include rotational effects have been described in Ref. 5. The rotation velocity is defined by

$$u = \frac{R_{ref}\Omega_\phi}{v_{thref}} = \Omega_N, \tag{10}$$

at the rotational gradient

$$u' = -\frac{R_{ref}}{v_{thref}} \frac{\partial \Omega_\phi}{\partial \psi} = -\frac{\partial \Omega_N}{\partial \psi}, \tag{11}$$

with the reference thermal velocity

$$v_{thref} = \sqrt{\frac{2T}{m}}. \tag{12}$$

The rotation adds terms to the drift of the particles

$$\frac{d\mathbf{X}}{dt} = \cdots + \frac{2mv_{||}}{ZeB}\Omega_\perp - \frac{m\Omega^2 R}{ZeB}\mathbf{b} \times \nabla R, \tag{13}$$

where the terms left out are the same as in Ref. 5 and Ω depicts the rotation frequency of the reference frame. The two terms are Coriolis and centrifugal drift, respectively. These have also been added in Ref. 5. Second, rotation causes a change of the background potential Φ. These are found using the quasi-neutrality condition

$$0 = \sum_{sp} Z_{sp} n_{R_0,sp} \exp\left(\frac{-Z_{sp}\langle\Phi\rangle}{T_{R,sp}}\right) \cdot \exp\left(\frac{m_{sp}\Omega^2\left(R^2 - R_0^2\right)}{T_{R,sp}}\right). \tag{14}$$

Third, the rotation modifies the trapping condition. With rotation, particles are trapped if

$$v_\perp^2 = \frac{v_{||}^2 - \frac{2}{m}\left(\mathcal{E}_H - \mathcal{E}_L\right)}{\frac{B_H}{B_L} - 1}, \tag{15}$$

where H and L stand for the high and low field side (LFS), respectively, and the species dependent centrifugal energy is defined as

$$\mathcal{E}(\theta) = Ze\Phi - \frac{1}{2} m_s \Omega^2 \left(R^2 - R_0^2\right). \tag{16}$$

Finally, also the source term of the gyrokinetic equation changes. The terms due to rotation are

$$S = \cdots - v_E \left[-\frac{m\Omega^2}{T} R_0 \frac{\partial R_0}{\partial \psi}\bigg|_\theta \nabla\psi + \frac{\mu B + \mathcal{E}}{T}\frac{\nabla T}{T} + \left(\frac{mv_{||}RB_t}{BT} + \frac{m\Omega}{T}\left[R^2 - R_0^2\right]\right)\nabla\omega_\phi \right] F_M. \tag{17}$$

Here, ω_ϕ is the rotation frequency of the plasma. As it is assumed that the rotation frequency of the frame and that of the plasma match at the chosen simulation, this means that the second term in the second line contains the product of rotation velocity and its gradient.

The simulations make also use of compressional effects, and there inclusion is described in Ref. 28.

As the density varies around the flux surface, the densities and density gradients $R/L_{n,s}$ given in Tables II and III are defined using density profiles at the LFS, $n_s(r, \theta = 0)$. Due to the centrifugal effects for the experimental rotation velocity at the inboard side of the tokamak ($\theta = \pi$), the densities drop to 0.992, 0.956, and 0.975 relative to the outboard side ($\theta = 0$), for deuterium, carbon, and electrons, respectively. The corresponding values for the density gradients are 0.983, 0.893, and 0.604.

The grid size in velocity space was $N_\mu = 16$ points for the magnetic moment, μ, and $N_{v_{||}} = 64$ for the parallel velocity. The number of points along the field lines differed for the two shots. Discharge 129064 was simulated with $N_s = 2208$ points divided over 23 rotations of the field line (except for $k_\theta\rho = 0.3$, where this resolution had to be increased), while for discharge 129061, 19 rotations of the field line are covered with $N_s = 1512$ points for low $k_\theta\rho$ and $N_s = 1008$ for higher values (≥ 0.6). Three species have been included in both discharges: deuterium, carbon, and electrons. In the second discharge, partially ionized tungsten ($Z = 39$) has been added as a trace species to investigate centrifugal effects on high-Z impurity transport. The actual experiments had no plasma facing components containing tungsten. Using high Z tiles in some parts is planned, which is an additional motivation for studying a tungsten trace. The time step was $5 \cdot 10^{-4}[v_{thref}/R_{ref}]$. The lithium in the second discharge has been neglected, as the contribution to the effective charge is small (i.e., $n_{Li}Z_{Li}^2/n_e \ll 1$).[29] A check if the solution is sufficiently converged has been performed for the first shot at $k_\theta\rho = 0.2$. The resolution of each "direction" (μ, $v_{||}$, s, t, n_{period}) was doubled in individual runs. The maximum deviation from the values of the default grid size for growth rate, frequency, and the ratio of heat to momentum flux (individually and sum) is 3%. Thus, good convergence of the calculated values is reached in the simulations.

Since rotation velocities vary in the experiment, as seen in Fig. 1, simulations are performed not only for the experimental value of the rotation velocity as given in Table I but

This article is copyrighted as indicated in the article. Reuse of AIP content is subject to the terms at: http://scitation.aip.org/termsconditions. Downloaded to IP: 198.125.231.54 On: Wed, 30 Sep 2015 20:20:01

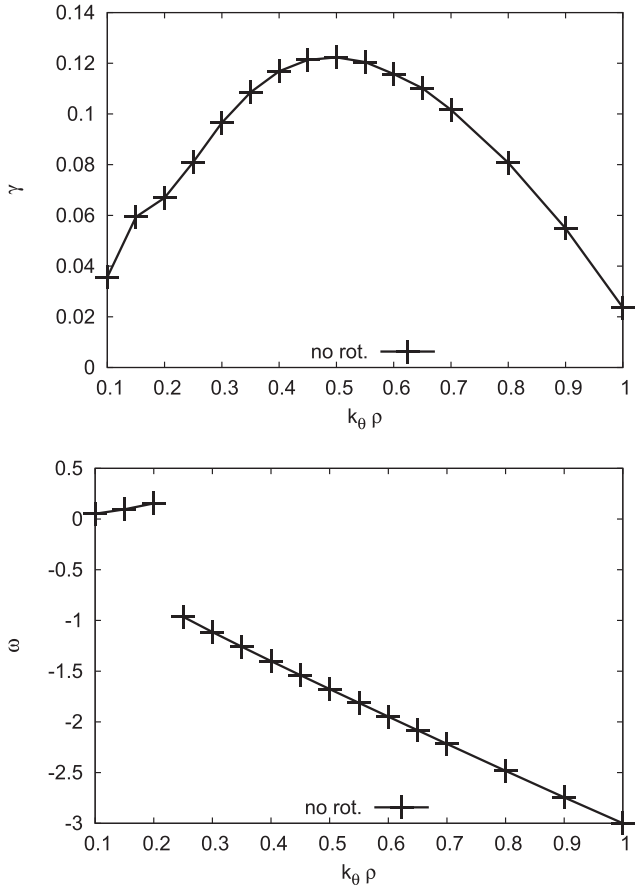

FIG. 3. Growth rate (top) and real frequency (bottom) vs. $k_\theta\rho$.

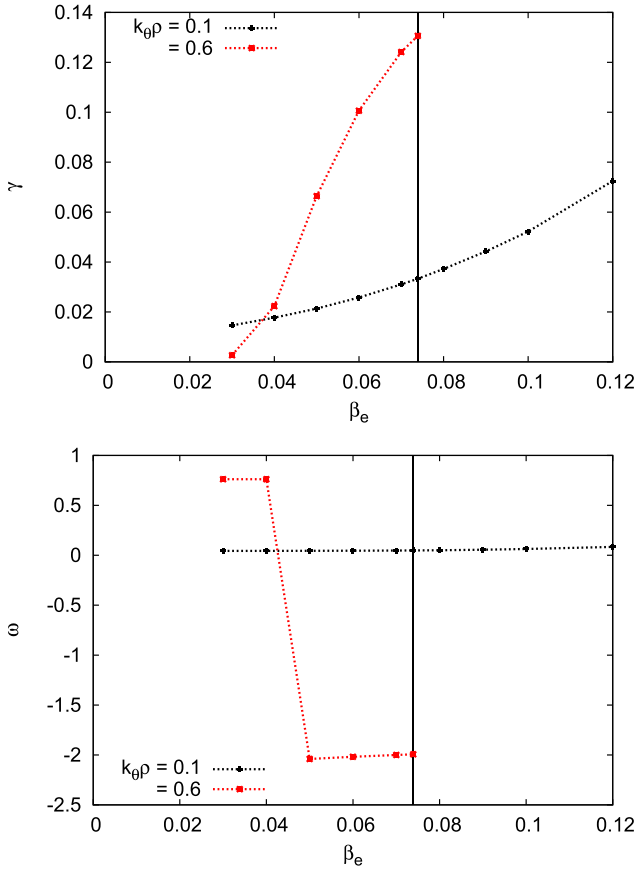

FIG. 4. Growth rate (top) and real frequency (bottom) vs. β_e for two different wave vectors. The vertical line shows the default β_e (given in Table I). The default case corresponds to the line for $u' + u$ (dashed, i.e., full rotational effects) of Fig. 8.

also for twice this value. This helps to have a rough upper bound.

III. MODES IN SHOT 129061

In this section, the second shot (129061) is considered. First, the nature of the instabilities and the impact of rotation are investigated.

Fig. 3 shows the growth rate (top) and the real frequency (bottom) as a function of $k_\theta\rho$. A negative frequency denotes a rotation in the electron diamagnetic direction. As can be seen from the figure that shows the frequency, two different modes are found in the $k_\theta\rho$ scan. The mode at higher $k_\theta\rho$ can be identified as a MTM, from its mode structure, parity, and sign of the frequency. For the same reasons, the second mode, at first, might appear to be a KBM, but scans over β_e (Fig. 4), R/L_{T_e} (Fig. 5), and ν_{ref} (Fig. 6) indicate that the situation is more complex.

The mode shows no clear onset at a finite β_e as expected for a KBM. Instead, the growth rate remains finite, even for small values of β_e. However, the β_e dependence gets stronger for values bigger than the experimental one. Due to this, we refine our identification of this mode to a hybrid ITG-KBM as discussed in Refs. 12 and 30.

The MTM mode shows a strong dependence upon β_e.[22] If β_e is reduced to approximately half the experimental value, then a transition to an ITG occurs.

Scans over the electron temperature gradient length R/L_{T_e} and the collision frequency are shown in Figs. 5 and 6, respectively. There is a strong increase of the MTM growth rate with R/L_{T_e} in NSTX.[31] Furthermore, as the core MTM is destabilized by collisions, a switch to another mode at lower collisionality is found. This seems to be an ITG mode. Interestingly, also higher values of the collisionality stabilize the MTM.

Having identified the modes, we now turn to investigating the influence of various rotation effects on the strength of the instabilities. Figure 7 shows the same data as Fig. 3, plus lines for the case with rotation while taking only Coriolis effects into account. The labels u, u', and $u' + u$ mean that a finite rotation velocity u, a rotational gradient u', and both have been included in the simulations, respectively. It can be seen immediately that there is little change in the real frequencies or growth rates of each mode, regardless of u or u'. Consequently, the value of $k_\theta\rho$, where the switch between the hybrid ITG-KBM and the MTM occurs, does not depend significantly on rotation.

This picture changes when full rotational effects (Coriolis and all centrifugal effects) are considered, as can be seen in Fig. 8. Values of the MTM growth rate increase about 10% for the experimental rotation values, while also the position of the maximum growth rate shifts to higher

This article is copyrighted as indicated in the article. Reuse of AIP content is subject to the terms at: http://scitation.aip.org/termsconditions. Downloaded to IP: 198.125.231.54 On: Wed, 30 Sep 2015 20:20:01

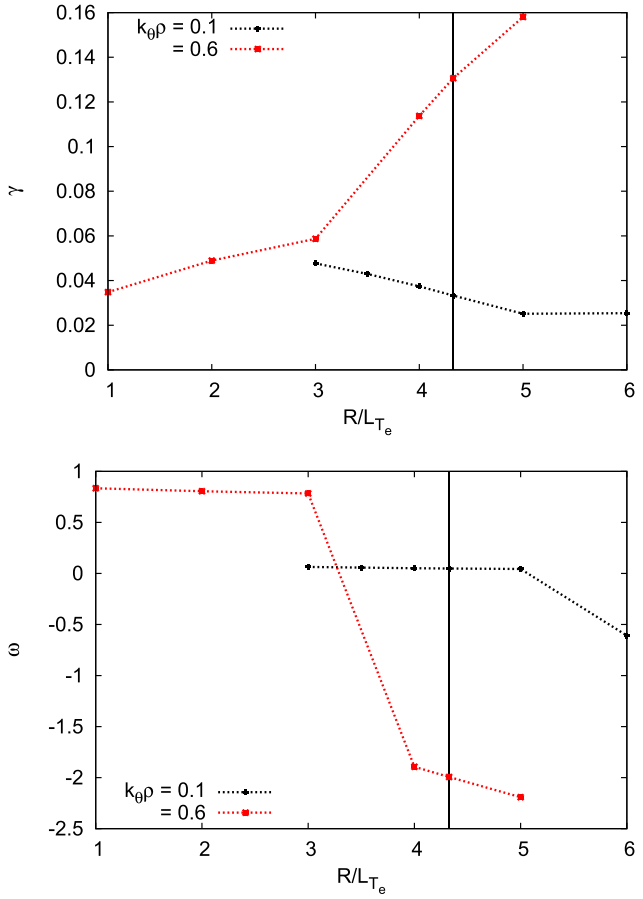

FIG. 5. Growth rate (top) and real frequency (bottom) vs. R/L_{T_e} for two different wave vectors. Please note that for this scan $\beta_e^{'}$ was not fixed. The vertical line shows the default R/L_{T_e} (given in Table III). The default case corresponds to the line for $u' + u$ (dashed, i.e., full rotational effects) of Fig. 8.

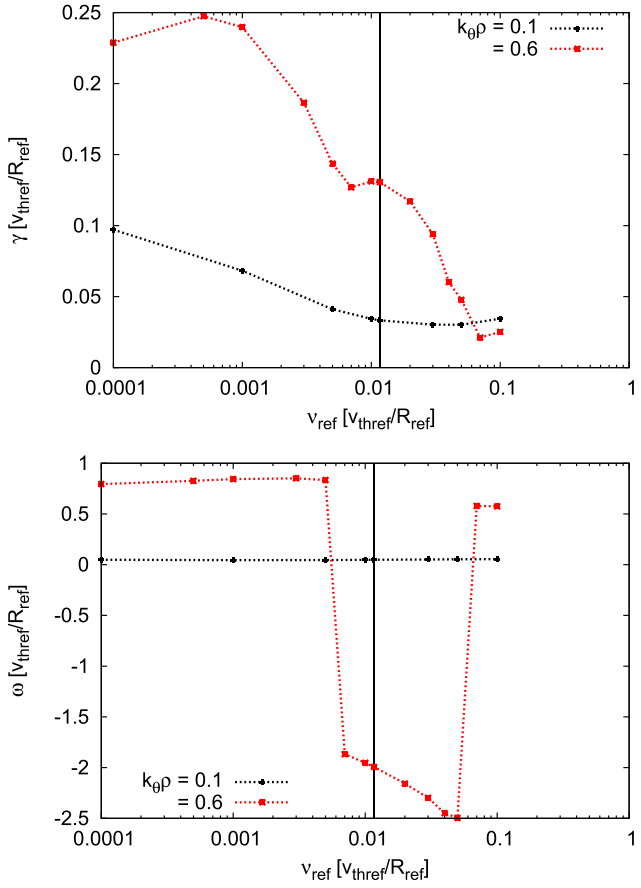

FIG. 6. Growth rate (top) and real frequency (bottom) vs. ν_{ref} for two different wave vectors. The vertical line shows the default ν_{ref} (from parameters given in Tables I and III). The default case corresponds to the line for $u' + u$ (dashed, i.e., full rotational effects) of Fig. 8.

wave numbers. The effect on the frequency is less pronounced. The hybrid ITG-KBM, however, is slightly stabilized. As a result, the wavenumber where mode dominance changes is shifted to lower $k_\theta\rho$ when the rotation velocity is increased. In the limit of twice the experimental rotation velocity ($u' + 2u$), the ITG-KBM is only apparent in the lowest $k_\theta\rho$ simulated.

To isolate the influence of the inertial terms on the growth rates, additional simulations were run artificially including or excluding terms associated with the various centrifugal effects. For example, Fig. 9 shows the response of the ITG-KBM mode ($k_\theta\rho = 0.1$) to rotation when including only the Coriolis drift (co), only centrifugal drift (cd), or a case that includes the modification in trapping, poloidal asymmetry of density, and source terms (tr) as discussed in Sec. II (Eqs. (13)–(17)). In this case, the dominant effect (albeit relatively small) appears to be due to the stabilization associated with the centrifugal drift, while the Coriolis drift and trapping effects have even smaller effect. We note that a decrease in growth rate with increasing rotation velocity was also found previously for electrostatic ITG modes.[5] In that case, the stabilization appeared to be due to both Coriolis and centrifugal drift terms, whereas the change in particle trapping and poloidal density variation was strongly destabilizing for similar rotation speeds ($u < 0.3$). Figure 10 shows the same for the microtearing mode ($k_\theta\rho = 0.7$). In this case, the growth rate is increased with rotation due to the changes associated with the particle trapping, poloidal density asymmetry, and source terms.

To conclude, analysis of the shot number 129061 shows the presence of a hybrid ITG-KBM and a MTM. Centrifugal effects were shown to change the growth rate on the order of 10%. In this case, the effect is relatively small since the Mach number of deuterium is not large, and the modes are largely supported by the main species. Impurity transport, due to the higher Mach number of the impurity species, and momentum transport react more strongly as we will see in Sections IV and V.

IV. PARTICLE TRANSPORT

As MTM only contributes to electron heat flux, this section will investigate the particle transport due to the hybrid ITG-KBM, which is shown to change strongly for the trace species, even if the growth rate and/or frequency do not. As electrons and deuterium have already been studied,[32,33] the focus will be on the intrinsic carbon impurity. We also consider a high-Z trace impurity which in this study we have chosen to be tungsten since

This article is copyrighted as indicated in the article. Reuse of AIP content is subject to the terms at: http://scitation.aip.org/termsconditions. Downloaded to IP: 198.125.231.54 On: Wed, 30 Sep 2015 20:20:01

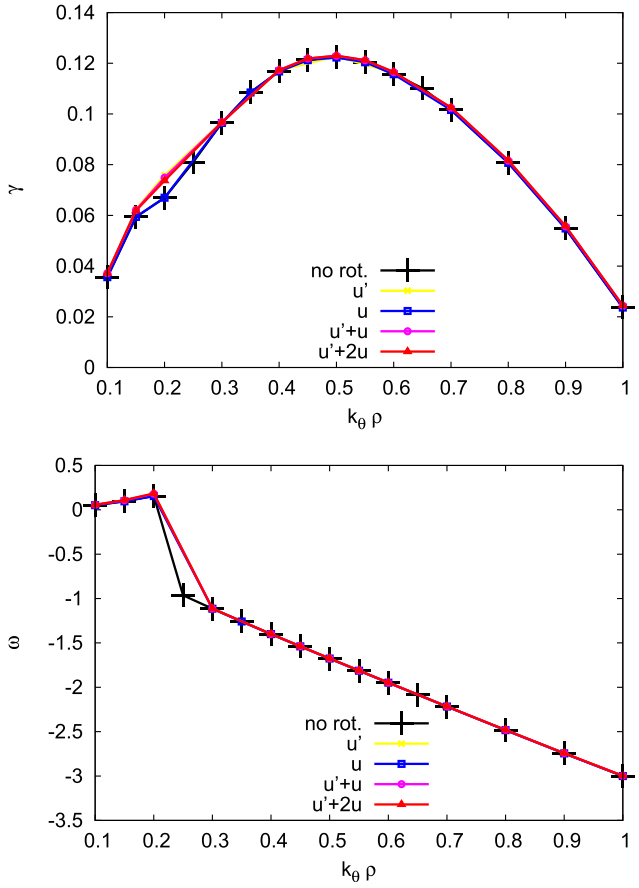

FIG. 7. Growth rate (top) and real frequency (bottom) vs. $k_\theta\rho$ for different combinations of rotations and rotational gradients ($u = 0.1362$ and $u' = 0.9099$). Only Coriolis effects have been included.

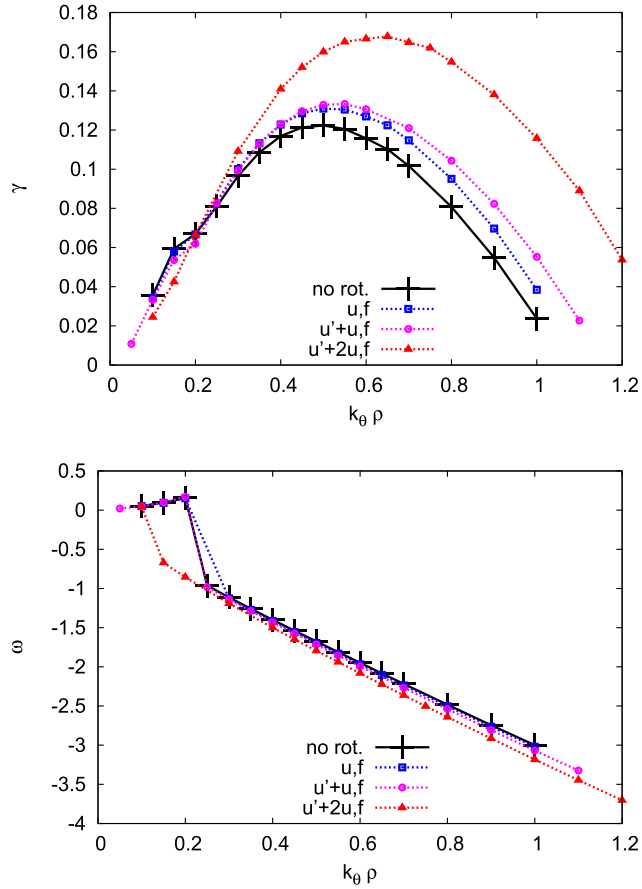

FIG. 8. Growth rate (top) and real frequency (bottom) vs. $k_\theta\rho$ for different combinations of rotations and rotational gradients ($u = 0.1362$ and $u' = 0.9099$). All the rotational effects have been included.

it is being considered as a possible plasma facing component in fusion reactors[34]). Also, we assume that the ITG-KBM will influence the particle and momentum transport, despite the lower growth rates compared to the microtearing mode.

The particle fluxes of carbon and tungsten (normalized to the electron heat flux) are shown in Fig. 11 for the hybrid ITG-KBM. For the case with no rotation, both carbon and tungsten fluxes are inward directed (negative). For carbon, this corresponds to down the gradient as it is locally hollow (see R/L_n in Table III), consistent with a strong diffusive component. As there is no tungsten density gradient, the finite tungsten particle flux is dominated by the curvature $+ E \times B$ compression pinch, which is proportional to impurity mass.[5] When including only the Coriolis drift, a finite rotation velocity has very little effect on the particle fluxes. However, a finite rotational gradient does drive an outward flux, an effect referred to as roto-diffusion. For tungsten, this drive is strong enough to change the flux direction from inward to outward, while for carbon it makes the fluxes less negative. Including centrifugal effects in the simulations makes little change to the carbon fluxes beyond the Coriolis and roto-diffusion effects, regardless of rotation or rotation shear. However, there is a much stronger influence on tungsten, as seen in Fig. 12. Centrifugal effects, when including only finite rotation (without shear), lead to a strong outward tungsten particle flux. With the addition of rotation shear, the tungsten particle fluxes exhibit a non-monotonic dependence, first decreasing and becoming strongly negative for experimental values of flow shear and then increasing and returning to approximately zero for twice the experimental flow shear. Similar dependencies are found when varying rotation while keeping rotation shear fixed at the experimental value. This can be seen in Fig. 13 where the particle flux of both carbon and tungsten as a function of the rotation velocity is shown for $k_\theta\rho = 0.1$. The scan shows that the carbon flux is relatively insensitive to changes in rotation. Tungsten, however, shows a clear nonlinear dependence with rotation velocity. For small rotation velocities ($u < 0.03$), an inward pinch increases nearly linearly. However, as rotation is increased further, the inward particle flux is eventually weakened, approaching zero for twice the experimental rotation. This might be explained by the behaviour of the variation in strength of convective and the rotodiffusive transport coefficient as rotation velocity is increased.[5] Comparing Figs. 11 and 12, one can also see that the centrifugal effects proportional to u cause a strong outward tungsten flux. That the flux is inward with rotation and rotational gradient suggests that effects proportional to $u \cdot u'$ are important.

This article is copyrighted as indicated in the article. Reuse of AIP content is subject to the terms at: http://scitation.aip.org/termsconditions. Downloaded to IP: 198.125.231.54 On: Wed, 30 Sep 2015 20:20:01

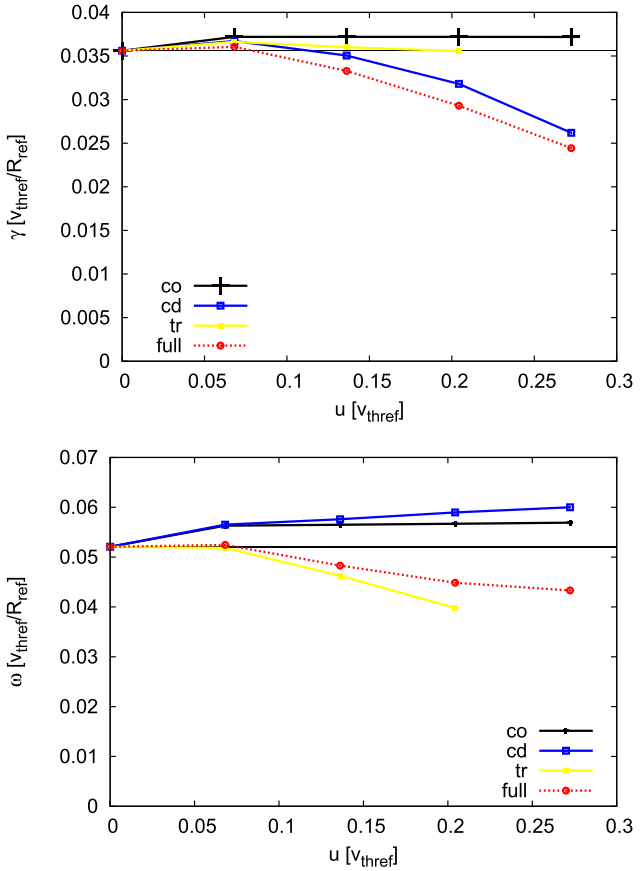

FIG. 9. Growth rate (top) and real frequency (bottom) vs. rotation velocity u for the ITG-KBM mode at $k_\theta\rho = 0.1$. The horizontal lines highlight the values for no rotation. The meaning of the labels is as follows: "co" Coriolis drift, "cd" centrifugal drift, "tr" centrifugal trapping and change in potential, "full" all three.

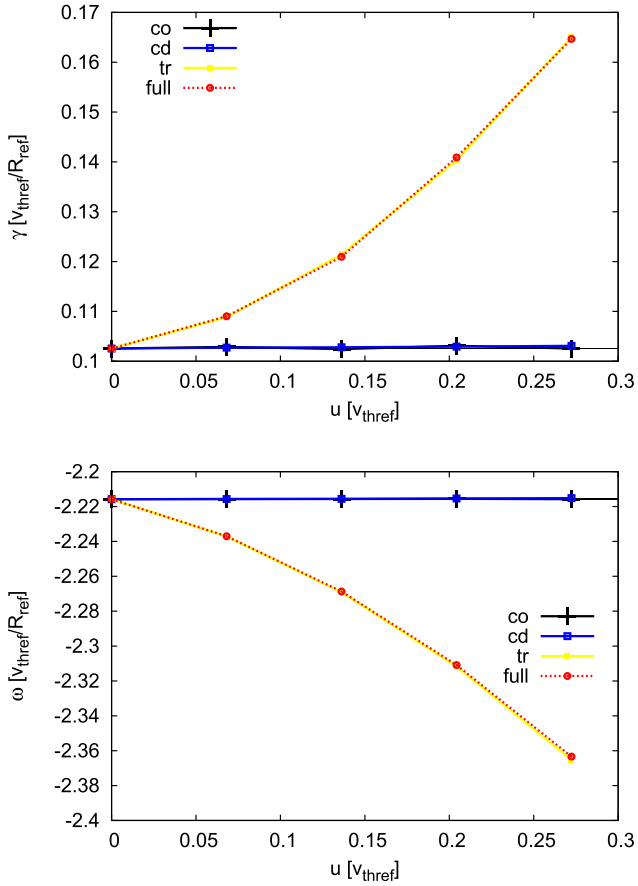

FIG. 10. Growth rate (top) and real frequency (bottom) vs. rotation velocity u for the MTM mode at $k_\theta\rho = 0.7$ (not 0.6). The horizontal lines highlight the values for no rotation. The meaning of the labels is as follows: "co" Coriolis drift, "cd" centrifugal drift, "tr" centrifugal trapping and change in potential, "full" all three.

The small flux without rotation means that the logarithmic density gradient $L_{n,W}$ needed to satisfy zero tungsten particle flux in the source-free core ($\Gamma_W = 0$) is almost zero, as can be seen in Table IV. With the experimental values for the rotation, the inward flux is stronger and thus a peaked density profile would be predicted. This is clearly unfavorable as the accumulation of high-Z impurities in the core can increase radiation losses and thus reduce confinement. However, given the complicated interplay between rotation and rotation gradient (which is similar to that found in Ref. 5 for ITG modes), this effect may very well be alleviated with a variation in rotation profiles, e.g., increasing the rotation velocity can reduce this problem.

Analogous to Table IV, the density gradient length, $R/L_{n,c}$, needed to satisfy zero carbon particle flux ($\Gamma_c = 0$ in the source-free core region) has been calculated from simulations using additional trace carbon species with different values of density ($R/L_{n,c} = \pm 5, 0$). Assuming a linear dependence of the flux on $R/L_{n,c}$, the offset and the declination can be computed, and from both the density gradient at which the flux is zero. The resulting $R/L_{n,c}$ should be an acceptable approximation, assuming the transport can be approximated by a linear function of $R/L_{n,c}$. This has been verified by calculating $R/L_{n,c}$ using an additional simulation where the density gradients of the bulk species have been halved. The resulting $R/L_{n,c} = -3.5$ is within 20% of the value obtained using the first method ($R/L_{n,c} = -2.8$).

Fig. 14 shows the calculated density gradient length, $R/L_{n,c}$, needed for zero carbon particle flux for various values of rotation and rotation shear. In the absence of a rotation gradient ($u' = 0$, top panel), the simulations predict a peaked carbon profile, regardless of rotation and inclusion of centrifugal effects. This is consistent with the inward (negative) carbon fluxes found in Figs. 11 and 12 for $u' = 0$.

The picture changes significantly if also the rotation gradient is included (bottom panel). In this case, roto-diffusion provides a strong outward particle flux. Therefore, a locally hollow profile ($R/L_{n,c} < 0$) is needed to obtain zero particle flux. If centrifugal effects are neglected (Coriolis only), the predicted gradient is $R/L_{n,c} \approx -0.85$ and is largely independent of rotation (u). Including centrifugal effects leads to an enhancement in the hollowing that increases with toroidal rotation. For the experimental rotation $u_{exp} = 0.14$, $R/L_{n,c} \approx -2.8$ is nearly three times bigger. This value of the density gradient is notably similar to the experimental value $R/L_{n,c-\mathrm{exp}} = -3.5$. If this effect is manifested in nonlinear simulations, it suggests that the locally inverted carbon

This article is copyrighted as indicated in the article. Reuse of AIP content is subject to the terms at: http://scitation.aip.org/termsconditions. Downloaded to IP: 198.125.231.54 On: Wed, 30 Sep 2015 20:20:01

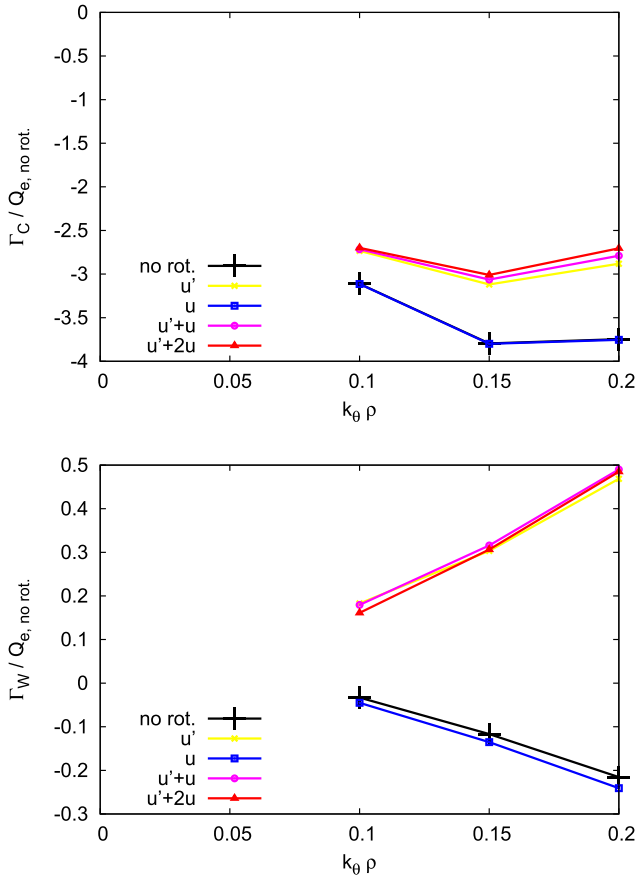

FIG. 11. Particle flux for carbon (top) and tungsten (bottom) as a function of $k_\theta\rho$. Only Coriolis effects have been included.

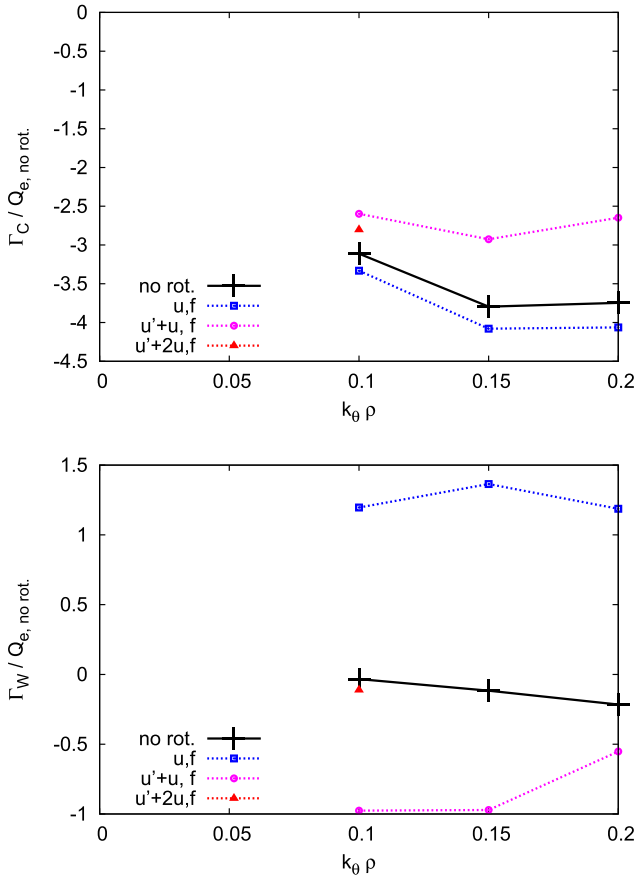

FIG. 12. Particle flux for carbon (top) and tungsten (bottom) as a function of $k_\theta\rho$. All rotational effects have been included. The case $u' + 2u$ has only one point as for higher $k_\theta\rho$ the mode switches.

profile (in this source-free region) is due to a balance between diffusive effects and the strong outward transport from both roto-diffusion and centrifugal effects for the ITG-KBM instability.

V. MOMENTUM TRANSPORT

The results for the momentum flux of the hybrid ITG-KBM is presented in this section.

Fig. 15 shows the momentum flux normalized to the ion (deuterium + carbon) heat flux for carbon and deuterium over $k_\theta\rho$ with only Coriolis effects. Without rotational gradient, the fluxes are small but finite, indicative of a residual stress. Both species show a similar response to rotation and rotation gradient, which is not unexpected due to the coupling through charge neutrality. Specifically, with a finite rotational gradient, there is an outwards directed diffusive flux of momentum ($\Pi \sim \chi_\phi u'$). The momentum fluxes change very little when including finite rotation, indicating that any momentum pinch ($\Pi \sim V_{pinch} u$) due to the Coriolis drift is very small. When including centrifugal effects (Fig. 16), there is also little change observed, except for the case of double rotation ($u' + 2u$). In this case, the flux is lower compared to the case with just the experimental rotation. This is not the case for carbon, where the flux is almost unaffected.

To better quantify the above effects, the momentum flux has been decomposed according to the model

$$\frac{\Pi_\phi^l}{Q_i^l}\frac{v_{thref}}{R_0} = \frac{2}{R/L_{T_i}}\frac{\chi_\phi}{\chi_i}\left[u' + \frac{R_0 V_{co}}{\chi_\phi}u + \frac{C^*}{\chi_\phi} + cuu'\right]. \quad (18)$$

Here, $Pr = \frac{\chi_\phi}{\chi_i}$ is the Prandtl number, $\frac{R_0 V_{co}}{\chi_\phi}$ the pinch coefficient, and $\frac{C^*}{\chi_\phi}$ the residual stress. The last term $c = c^*/\chi_\phi$ has

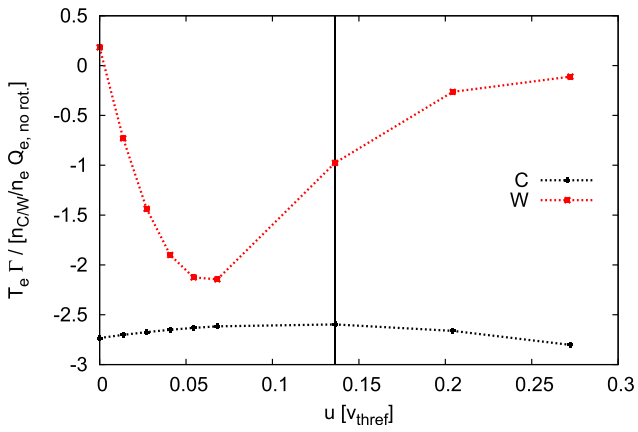

FIG. 13. Particle flux for carbon and tungsten as a function of rotation velocity u. The scan has been done with Coriolis and centrifugal effects at $k_\theta\rho = 0.1$.

This article is copyrighted as indicated in the article. Reuse of AIP content is subject to the terms at: http://scitation.aip.org/termsconditions. Downloaded to IP: 198.125.231.54 On: Wed, 30 Sep 2015 20:20:01

TABLE IV. Density gradients for zero tungsten and carbon particle flux at $k_\theta \rho = 0.1$. If the simulation included rotation, then all effects have been activated.

Rotation	$R/L_{n,W}\|_{\Gamma_W=0}$
No	0.008
Yes	1.112

been added (compared to Ref. 35) as a check if the effects related to both the rotation and rotation gradient might be important, as noted in Ref. 5. Π_ϕ^l and Q_i^l here refer to the sum of the deuterium and carbon momentum and heat fluxes, respectively. These have been calculated from simulations using all combinations of zero or experimental rotation and rotation gradient. Thus, we obtain a linear system with the transport coefficients as unknowns that can be solved for.

The resulting transport coefficients are shown in Fig. 17. The Prandtl number for the ITG-KBM mode is predicted to be very small, $Pr \sim 0.1 - 0.2$, which is much smaller than values ($Pr \sim 0.7 - 1.0$) typical for electrostatic ITG, TEM, or KBM instabilities (see, e.g., Ref. 36). The predicted Coriolis pinch without centrifugal effects is also small $\frac{R_0 V_{co}}{\chi_\phi} \sim -0.1$, but this has been predicted

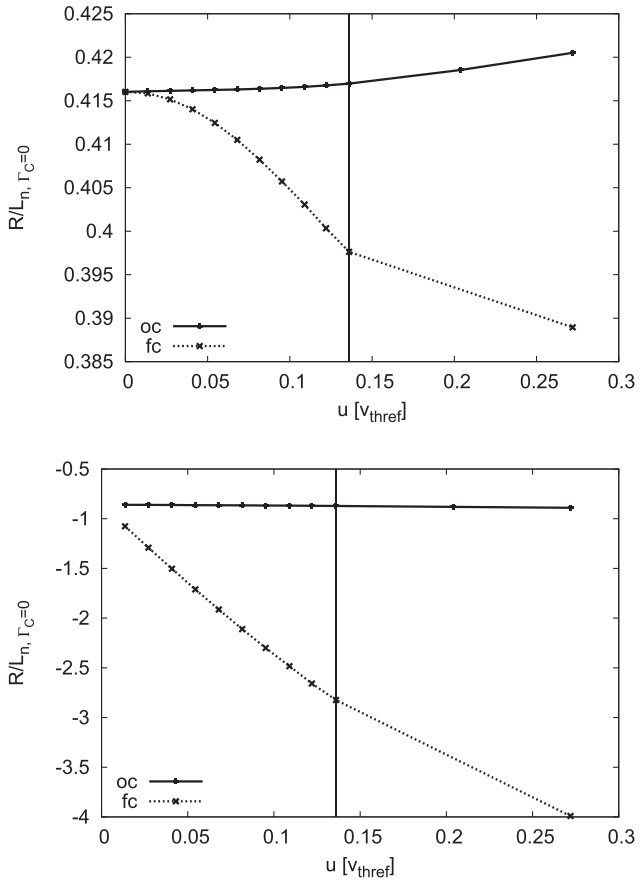

FIG. 14. Density gradient length for zero carbon particle flux. With $u' = 0$ (top) and the experimental value $u' = 0.9099$ (bottom), for the case with only the Coriolis effects (oc) and all the rotational effects (fc).

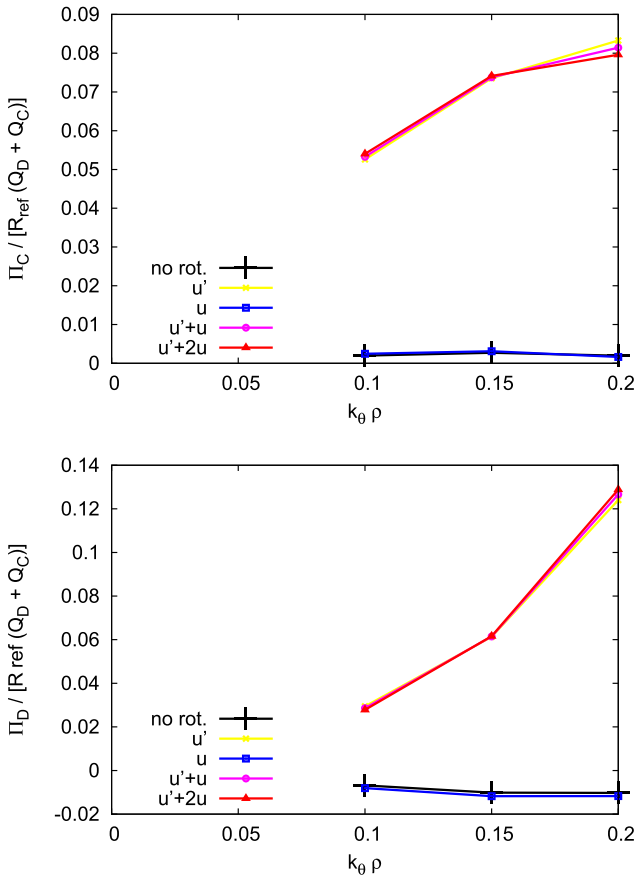

FIG. 15. Momentum flux normalized to ion (deuterium + carbon) heat flux for carbon (top) and deuterium (bottom). Only Coriolis effects have been included.

previously for KBM instability at higher aspect ratio.[20] The strength of the Coriolis pinch is roughly doubled when including centrifugal effects (blue dashed line). The overall small pinch from ITG-KBM apparently cannot explain the larger momentum pinches measured in similar NSTX H-mode plasmas ($\frac{R_0 V_\phi}{\chi_\phi} \sim (-1) - (-7)$).[11] Therefore, we look at the other possible contributions in Eq. (18).

There is a finite residual stress predicted, although it's relative magnitude is no larger than the pinch contribution. This residual stress is due to an up-down asymmetry introduced by the finite derivative of the vertical position Z_0 with respect to radial coordinate (dZ_{mil}) in the geometry description. This has been verified by additional simulations that show the residual stress is reduced by four orders of magnitude if dZ_{mil} is reduced to zero.

The residual stress should not change when including centrifugal effects, as this describes the flux without rotation. The Prandtl number also does not change. Thus, those two have not been computed again with full rotational effects.

The strongest contribution to the momentum fluxes appears to come from the $u \cdot u'$ coefficient when including centrifugal effects. In the absence of centrifugal effects, this term is very small and should be identically zero in the limit that the various terms in Eq. (18) can be decomposed exactly as linear contributions. However, with centrifugal effects

This article is copyrighted as indicated in the article. Reuse of AIP content is subject to the terms at: http://scitation.aip.org/termsconditions. Downloaded to IP: 198.125.231.54 On: Wed, 30 Sep 2015 20:20:01

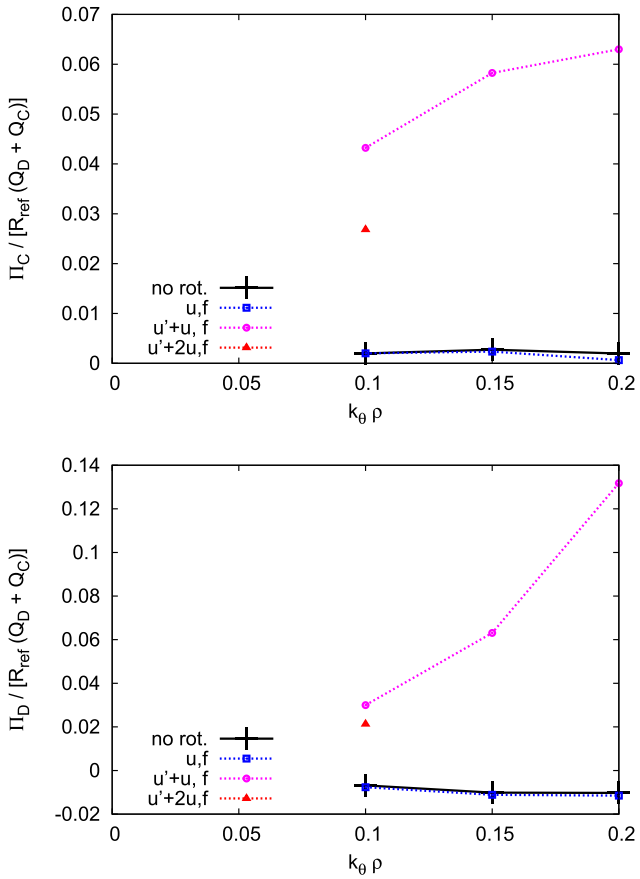

FIG. 16. Momentum flux normalized to ion (deuterium + carbon) heat flux for carbon (top) and deuterium (bottom). All rotational effects have been included.

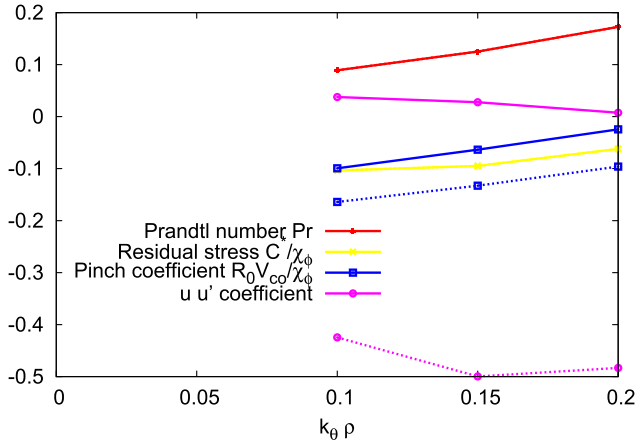

FIG. 17. The transport coefficients vs. $k_\theta \rho$ in the hybrid KBM range. Full lines refer to only Coriolis effects, while dashed line includes also centrifugal effects. Prandtl number and residual stress have not been computed with centrifugal effects.

included, this term provides an inward flux contribution that is ~3 times larger than the Coriolis pinch contribution. This additional centrifugal effect will be explored more carefully in future work to determine whether it can provide a possible explanation of the observed momentum pinches in NSTX H-modes.

VI. CONCLUSIONS

The influence of centrifugal effects on microstability (including centrifugal drifts, change of background potential, change of trapping condition, and change of source term in the gyrokinetic equation) has been investigated using the GKW code for relatively high-beta NSTX H-mode plasmas. The linear, flux-tube simulations predict the presence of both MTM and hybrid ITG-KBM electromagnetic instabilities in the outer core ($r/a = 0.7$), inferred from mode structure and parameter scans. Both instabilities respond weakly to changes in rotation and rotation shear for the experimental parameters investigated, although the MTM growth rates appear to be strengthened for values of rotation increased beyond the local values ($u > 0.1$), specifically due to centrifugal effects.

Quasi-linear fluxes have been calculated for the ITG-KBM modes to estimate what effect they might have on impurity and rotation profiles. The assumption has been made that the ITG-KBM effects are present even though in this case the growth rates are weaker than the microtearing mode (which contributes only to electron heat flux). This assumption will be tested in future nonlinear simulations. The carbon density gradient predicted in the absence of a source ($\Gamma_c \approx 0$, appropriate for these core conditions) is found to be locally hollow ($R/L_{nc,C} < 0$). This prediction is dependent on including finite rotation shear ($u' > 0$) and is strengthened when centrifugal effects are included. These results provide a possible explanation for the inverted carbon profile measured at this location,[18] which could not be explained by neoclassical theory (as is usually the case). In constrast, if only Coriolis effects are included ($u' = 0$), an inward pinch and peaked carbon profile ($R/L_{nc,C} > 0$) are calculated, inconsistent with experimental results.

For a trace high-Z impurity (assumed here to be tungsten), the influence of rotation when including centrifugal effects is strongly non-monotonic. For the experimental values of this investigation, a strong inward pinch is predicted. However, this high-Z impurity flux can be reduced considerably for either weaker or stronger rotation. This effect was predicted previously for simpler geometry[5] and has been extended here to realistic low aspect ratio geometry, assuming the presence of a trace tungsten species. High-Z impurity transport and its sensitivity to rotation will be investigated in future NSTX-Upgrade[37] experiments.

When including all rotation effects, the simulated momentum flux is outward, consistent with the central torque deposition from NBI heating. However, the diffusive and Coriolis pinch contributions predicted from the ITG-KBM simulations are relatively small, with $Pr \sim 0.1 - 0.2$ and $\frac{R_0 V_{co}}{\chi_\phi} \approx 0.1 - 0.2$. We note in the present investigation that the strength of the pinch is enhanced when centrifugal effects are included, although they remain much smaller than experimental observations in similar NSTX H-mode plasmas.[11] However, there is an additional contribution to the inward momentum flux from a term proportional to the product of uu', which is ~3 times bigger than the Coriolis pinch contribution. This additional mechanism may provide a possible explanation for the experimental observations and will be explored in future work.

This article is copyrighted as indicated in the article. Reuse of AIP content is subject to the terms at: http://scitation.aip.org/termsconditions. Downloaded to IP: 198.125.231.54 On: Wed, 30 Sep 2015 20:20:01

Within this paper, the rational gradient has not been changed, only switched on/off for some of the scans. At least in the inside of the plasma, there seems to be a relation of rotation and its gradient in NSTX. It would thus be desirable to check how transport is affected, when both are changed according to this relation. We leave this for a future investigation.

ACKNOWLEDGMENTS

We thank R. E. Bell and B. P. LeBlanc for providing the experimental fits for the discharges analyzed in this paper and F. Scotti for the TRANSP runs, from which the profiles for the simulations have been used. We thank F. Scotti also for helpful comments.

[1]R. E. Waltz, G. M. Staebler, J. Candy, and F. L. Hinton, Phys. Plasmas **14**, 122507 (2007).
[2]R. R. Dominguez and G. M. Staebler, Phys. Fluids B **5**, 3876 (1993).
[3]P. J. Catto, M. N. Rosenbluth, and C. S. Liu, Phys. Fluids **16**, 1719 (1973).
[4]A. G. Peeters, D. Strintzi, Y. Camenen, C. Angioni, F. J. Casson, W. A. Hornsby, and A. P. Snodin, Phys. Plasmas **16**, 042310 (2009).
[5]F. J. Casson, A. G. Peeters, C. Angioni, Y. Camenen, W. A. Hornsby, A. P. Snodin, and G. Szepesi, Phys. Plasmas **17**, 102305 (2010); Erratum **19**, 099902 (2012).
[6]C. Angioni, R. M. McDermott, F. J. Casson, E. Fable, A. Bottino, R. Dux, R. Fischer, Y. Podoba, T. Pütterich, F. Ryter, E. Viezzer, and ASDEX Upgrade Team, Phys. Rev. Lett. **107**, 215003 (2011).
[7]Y. Camenen, A. Bortolon, B. P. Duval, L. Federspiel, A. G. Peeters, F. J. Casson, W. A. Hornsby, A. N. Karpushov, F. Piras, O. Sauter, A. P. Snodin, G. Szepesi, and TCV Team, Plasma Phys. Controlled Fusion **52**, 124037 (2010).
[8]M. Ono, S. M. Kaye, Y.-K. M. Peng, G. Barnes, W. Blanchard, M. D. Carter, J. Chrzanowski, L. Dudek, R. Ewig, D. Gates *et al.*, Nucl. Fusion **40**, 557 (2000).
[9]Y-K. M. Peng and D. J. Strickler, Nucl. Fusion **26**, 769 (1986).
[10]Y.-K. M. Peng, Phys. Plasmas **7**, 1681 (2000).
[11]S. M. Kaye, W. Solomon, R. E. Bell, B. P. LeBlanc, F. Levinton, J. Menard, G. Rewoldt, S. Sabbagh, W. Wang, and H. Yuh, Nucl. Fusion **49**, 045010 (2009).
[12]W. Guttenfelder, J. L. Peterson, J. Candy, S. M. Kaye, Y. Ren, R. E. Bell, G. W. Hammett, B. P. LeBlanc, D. R. Mikkelsen, W. M. Nevins, and H. Yuh, Nucl. Fusion **53**, 093022 (2013).
[13]F. J. Casson, R. M. McDermott, C. Angioni, Y. Camenen, R. Dux, E. Fable, R. Fischer, B. Geiger, P. Manas, L. Menchero, G. Tardini, and ASDEX Upgrade Team, Nucl. Fusion **53**, 063026 (2013).
[14]L. Delgado-Aparicio, D. Stutman, K. Tritz, M. Finkenthal, S. Kaye, R. Bell, R. Kaita, B. LeBlanc, F. Levinton, J. Menard, S. Paul, D. Smith, and H. Yuh, Nucl. Fusion **49**, 085028 (2009).
[15]L. Delgado-Aparicio, D. Stutman, K. Tritz, F. Volpe, K. L. Wong, R. Bell, M. Finkenthal, E. Fredrickson, S. P. Gerhardt, S. Kaye, B. LeBlanc, J. Menard, S. Paul, and L. Roquemore, Nucl. Fusion **51**, 083047 (2011).
[16]D. J. Clayton, K. Tritz, D. Stutman, M. Finkenthal, S. M. Kaye, D. Kumar, B. P. LeBlanc, S. Paul, and S. A. Sabbagh, Plasma Phys. Controlled Fusion **54**, 105022 (2012).
[17]R. Maingi, T. H. Osborne, B. P. LeBlanc, R. E. Bell, J. Manickam, P. B. Snyder, J. E. Menard, D. K. Mansfield, H. W. Kugel, R. Kaita, S. P. Gerhardt, S. A. Sabbagh, and F. A. Kelly, Phys. Rev. Lett. **103**, 075001 (2009).
[18]F. Scotti, V. A. Soukhanovskii, R. E. Bell, S. Gerhardt, W. Guttenfelder, S. Kaye, R. Andre, A. Diallo, R. Kaita, B. P. LeBlanc, M. Podestá, and NSTX Team, Nucl. Fusion **53**, 083001 (2013).
[19]S. M. Kaye, S. Gerhardt, W. Guttenfelder, R. Maingi, R. E. Bell, A. Diallo, B. P. LeBlanc, and M. Podestá, Nucl. Fusion **53**, 063005 (2013).
[20]T. Hein, C. Angioni, E. Fable, J. Candy, and A. G. Peeters, Phys. Plasmas **18**, 072503 (2011).
[21]W. Guttenfelder, J. Candy, S. M. Kaye, W. M. Nevins, E. Wang, J. Zhang, R. E. Bell, N. A. Crocker, G. W. Hammett, B. P. LeBlanc, D. R. Mikelsen, Y. Ren, and H. Yuh, Phys. Plasmas **19**, 056119 (2012).
[22]W. Guttenfelder, J. Candy, S. M. Kaye, W. M. Nevins, R. E. Bell, G. W. Hammett, B. P. LeBlanc, and H. Yuh, Phys. Plasmas **19**, 022506 (2012).
[23]W. Guttenfelder, J. Candy, S. M. Kaye, W. M. Nevins, E. Wang, R. E. Bell, G. W. Hammett, B. P. LeBlanc, D. R. Mikkelsen, and H. Yuh, Phys. Rev. Lett. **106**, 155004 (2011).
[24]H. Doerk, F. Jenko, M. J. Pueschel, and D. R. Hatch, Phys. Rev. Lett. **106**, 155003 (2011).
[25]J. Candy and R. E. Waltz, J. Comput. Phys. **186**, 545 (2003).
[26]A. G. Peeters, Y. Camenen, F. J. Casson, W. A. Hornsby, A. P. Snodin, D. Strintzi, and G. Szepesi, Comput. Phys. Commun. **180**, 2650 (2009).
[27]R. L. Miller, M. S. Chu, J. M. Greene, Y. R. Lin-Liu, and R. E. Waltz, Phys. Plasmas **5**, 973 (1998).
[28]G. Szepsi, "Derivation of the fully electro-magnetic, non-linear, gyrokinetic Vlasov–Maxwell equations in a rotating frame of reference for GKW with Lie transform perturbation method," (unpublished).
[29]M. Podestá, R. E. Bell, A. Diallo, B. P. LeBlanc, F. Scotti, and NSTX Team, Nucl. Fusion **52**, 033008 (2012).
[30]E. A. Belli and J. Candy, Phys. Plasmas **17**, 112314 (2010).
[31]S. Moradi, I. Pusztai, W. Guttenfelder, T. Fülöp, and A. Molln, Nucl. Fusion **53**, 063025 (2013).
[32]Y. Camenen, A. G. Peeters, C. Angioni, F. J. Casson, W. A. Hornsby, A. P. Snodin, and D. Strintzi, Phys. Plasmas **16**, 012503 (2009).
[33]S. Moradi, I. Pusztai, A. Molln, and T. Fülöp, Phys. Plasmas **19**, 032301 (2012).
[34]G. F. Matthews, M. Beurskens, S. Brezinsek, M. Groth, E. Joffrin, A. Loving, M. Kear, M.-L. Mayoral, R. Neu, P. Prior, V. Riccardo, F. Rimini, M. Rubel, G. Sips, E. Villedieu, P. de Vries, M. L. Watkins, and EFDA-JET Contributors, Phys. Scr. **T145**, 014001 (2011).
[35]Y. Camenen, Y. Idomura, S. Jolliet, and A. G. Peeters, Nucl. Fusion **51**, 073039 (2011).
[36]D. Strintzi, A. G. Peeters, and J. Weiland, Phys. Plasmas **15**, 044502 (2008).
[37]J. E. Menard, S. Gerhardt, M. Bell, J. Bialek, A. Brooks, J. Canik, J. Chrzanowski, M. Denault, L. Dudek, D. A. Gates *et al.*, Nucl. Fusion **52**, 083015 (2012).

This article is copyrighted as indicated in the article. Reuse of AIP content is subject to the terms at: http://scitation.aip.org/termsconditions. Downloaded to IP: 198.125.231.54 On: Wed, 30 Sep 2015 20:20:01